EFFECTS OF STATIC HETEROGENEITY ON THE PARALLEL-SEQUENTIAL-SUPEREXCHANGE MECHANISM FOR THE PRIMARY CHARGE SEPARATION IN BACTERIAL PHOTOSYNTHESIS

M. Bixon,[1] Joshua Jortner,[1] and M.E. Michel-Beyerle[2]
[1]School of Chemistry, Tel Aviv University, Tel Aviv 69978, Israel.
[2]Institut für Physikalische und Theoretische Chemie, Technische Universität München, Lichtenbergstr. 4, D-85748 Garching, Germany.

Key Words: Primary charge separation, Ni-Reaction center, RC mutants, Heterogeneity.

1. Introduction

Until the early 1990's, the experimental psec and subpsec data for the kinetics of the primary charge separation process in the photosynthetic RC were interpreted in terms of a single lifetime for each of the electronically excited singlet states of the bacteriochlorophyll dimer ($^1P^*$) and the ion pairs [1-4]. This approach seemed to indicate that heterogeneity effects on the kinetics are minor. This physical situation pointed towards the possibility that the dynamics in membrane proteins is drastically different from that in globular proteins [5-7], where low-temperature chemical dynamics, e.g., the recombination of CO to the heme site of myglobin, is dominated by a nonexponential heterogeneous kinetics [5-7]. Of course, heterogeneous kinetics, involving static inhomogeneity effects, indicates the existence of distinct microenvironments (for the relevant prosthetic groups involved in the reaction), which do not interconvert on the relevant time scale of the dynamic process. The existence of such static distribution of microenvironments, which is ubiquitous in globular proteins, results in a static distribution of the energetics, nuclear Franck-Condon factors or/and the electronic couplings which determine the rates. The apparent absence of inhomogeneous kinetics [1-4] for ET in the photsynthetic RC was surprising. With the refinements of the experimental techniques, evidence for inhomogeneous kinetics in the bacterial RC started emerging, being originally inferred from the dependence of the kinetics on the probing wavelength [8,9]. Recently, long-time tails were observed in the decay of $^1P^*$ as interrogated by stimulated emission and in fluorescence upconversion [10-13]. The decay of $^1P^*$ in the wild type reaction center could be fit by a biexponential with $\tau_1 = 2.6$ ps and $\tau_3 = 12$ ps with relative amplitudes of $A_3/A_1 \sim 0.15$ [10,11]. A similar behavior is exhibited for chemically modified RCs, e.g., for the 13²-OH-Ni-bacteriochlorophyll (Ni-B) → bacteriochlorophyll (B) substituted RC [14-16], where $\tau_1 = 2.5$ psec, $\tau_3 =$

7 psec and $A_3/A_1 \sim 0.4$ at T = 285 K. The biexponential pattern prevails also for a variety of local mutants with A_3/A_1 being considerably larger [10,11,17-19]. Structural heterogeneity may result in a continuous (or bimodal) distribution of the energy gaps and/or the reorganization energies and/or the electronic couplings. Experimental information on the spread of the energy of the P^+BH^- ion pair state relative to $^1P^*$ has become accessible from the temperature dependence of delayed fluorescence due to recombination of the ion pairs and the magnetic field effect therein [20]. This spread was characterized by a Gaussian distribution with a width parameter $\sigma = 400\ cm^{-1}$ (i.e., the FWHM being $2(2\ell n2)^{1/2}\sigma$) [20]. Concurrently, theoretical expressions were provided [11,21] for the ET rates in an inhomogeneously broadened (dispersive) system.

An outstanding problem in the understanding of the primary charge separation from $^1P^*$ to H across the A branch of the bacterial photosynthetic RC pertains to its mechanism [22-45]. We have advanced the parallel sequential-superexchange mechanism [43-45] for the primary ET, which provides a unified scheme that includes both the unistep superexchange mechanism and the two-step sequential mechanism as limiting cases. Although substantial experimental evidence for the dominance of the sequential mechanism in the native (N) RC at room temperature (T = 280-300 K) is available [10,14,38-42], the superexchange route is of some significance at low temperature native RC [43-45], is important for most single-site mutants at low temperature [45] and may be dominating for mutants with extreme values of the energy gap [45]. The merging between the parallel sequential-superexchange routes is of considerable interest, providing information and experimental guidance for:

(1) The energy gap dependence of the (averaged) initial decay times of $^1P^*$.
(2) The nature of the temporal nonexponential decay pattern of $^1P^*$.
(3) The energy gap dependence of the quantum yield for charge separation.
(4) The relative contribution of the parallel mechanisms (i.e., sequential and superexchange) to the initial decay times, to the pattern of the temporal decay of $^1P^*$ and to the quantum yield for a broad range of energy gaps.

The systems we explore correspond to:

(i) the native (N) RC ($\Delta G_1 \simeq -500\ cm^{-1}$) [42,45-47];
(ii) the Ni-B chemically substituted RC ($\Delta G_1 = -1500\ cm^{-1}$ [14-16]) corresponding to the lowest value of ΔG_1;
(iii) some other chemically engineered RCs [42];
(iv) the single-site 'good' [45,47] mutants [10,11,17,18], for which geometrical changes are minimized and the perturbation corresponds to $^1P^*/P^+$, while the perturbations of the prosthetic

groups of B and H are minor ($\Delta G_1 \simeq -1100$ cm^{-1} to 200 cm^{-1});

(v) triple mutants [19] ($\Delta G_1 \simeq 1000$ cm^{-1}), which are characterized by the largest value of ΔG_1.

The ΔG_1 scale spans the range of 2500 cm^{-1} (8 kcal/mol).

2. The parallel sequential-superexchange mechanism

The kinetic scheme for this mechanism [43-45] (Fig. 1) consists of:

(i) the sequential route

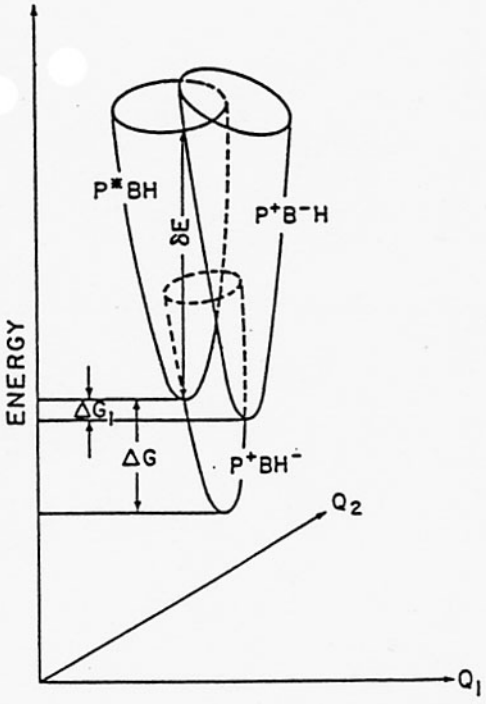

Fig. 1. Schematic potential energy surfaces for the primary charge separation in the RC.

$$^1P^*BH \underset{k_{-1}}{\overset{k_1}{\rightleftharpoons}} P^+B^-H \xrightarrow{k_2} P^+BH^- \qquad (1)$$

(ii) the superexchange route

$$^1P^*BH \underset{k_-}{\overset{k}{\rightleftharpoons}} P^+BH^- \qquad (2)$$

(iii) quinone reduction

$$P^+BH^-Q \xrightarrow{k_Q} P^+BHQ^- \quad (3)$$

(iv) internal conversion of the dimer

$$^1P^*BH \xrightarrow{k_d} PBH \quad (4)$$

(v) recombination of ion pairs

$$P^+B^-H \xrightarrow{k_R} PBH \quad (5)$$

$$P^+BH^- \xrightarrow{k_S} PBH \quad (6)$$

$$P^+BH^- \xrightarrow{k_T} {}^3P^*BH \ . \quad (7)$$

The theoretical description for the ET rates will be given in terms of the multiphonon nonadiabatic theory, which expresses the ET rate in the form $k = (2\pi/\hbar)V^2F$, where V is the electronic coupling and F is the Franck-Condon factor. The validity conditions for the applicability of this simple scheme, which we recently discussed [43-45], are:

1) The applicability of the nonadiabatic limit, which for characteristic parameters for the RC imply that [44] $V < 70\ cm^{-1}$ at $T = 300$ K. This relation, which is inferred from an a posteriori analysis, is obeyed for the ultrafast ET process and for all the subsequent ET reactions in the RC.
2) Insensitivity of the ET rates to medium dynamics. This state of affairs can be realized under two circumstances. (i) Fast medium relaxation dynamics. (ii) Activationless ET. Case (ii) is relevant for the description of the ultrafast primary ET processes. We have recently demonstrated [48] that activationless ET cannot be described in terms of the diffusion towards a point sink at the intersection of the potential nuclear surface at the minimum of the initial nuclear surface (for the medium modes). Rather, for activationless ET the microscopic ET rates are insensitive (within a numerical factor of ~ 2) to the distribution of the initial vibrational states [48]. Accordingly, the (activationless) primary ET processes in the RC are not controlled by medium dynamics and can be reasonably well described in terms of the conventional ET rate from an equilibrated vibrational manifold.

The four microscopic primary ET rate constants in Eqs. (1) and (2) are:

The superexchange rate:

$$k = \left(\frac{2\pi}{\hbar}\right)(V_{PB}V_{BH}/\delta E)^2 F(\lambda,\omega_m,S_c,\hbar\omega_c,\Delta G,T) \tag{8}$$

The first sequential rate:

$$k_1 = \left(\frac{2\pi}{\hbar}\right) V_{PB}^2\, F(\lambda_1,\hbar\omega_m,S_c,\hbar\omega_c,\Delta G_1,T) \tag{9}$$

The reverse rate:

$$k_{-1} = k_1 \exp(-\Delta G_1/k_B T) \tag{10}$$

The second sequential rate:

$$k_2 = \left(\frac{2\pi}{\hbar}\right) V_{BH}^2\, F(\lambda_2,\hbar\omega_m,S_c,\hbar\omega_c,\Delta G_2,T)\,. \tag{11}$$

The electronic couplings, the energey gaps and the nuclear coupling parameters which determine the rates are defined in Table 1. The Franck-Condon factors are

$$F(\lambda,\hbar\omega_m,S_c,\hbar\omega_c,\Delta G,T) = \sum_{n=0}^{\infty} F_m(\Delta G - n\hbar\omega_c)F_c(n) \tag{12}$$

with the medium contributions

$$F_m(\Delta E) = (\hbar\omega_m)^{-1}\left(\frac{\bar{\nu}+1}{\bar{\nu}}\right)^{p/2} \exp[-S_m(2\bar{\nu}+1)]I_p(2S_m[\bar{\nu}(\bar{\nu}+1)]^{1/2}), \tag{13}$$

where $\bar{\nu} = [\exp(\hbar\omega_m/k_B T)-1]^{-1}$ is the thermal population of the mode, $p = \Delta G/\hbar\omega_m$, $S_m = \lambda/\hbar\omega_m$ and $I_p(\cdot)$ is the modified Bessel function of order p. The intramolecular high-frequency contribution is

$$F_c(n) = \exp(-S_c)\, S_c^n/n!\,. \tag{14}$$

Table 1. Input data for kinetic modelling. Data assembled in reference 45 and references are quoted therein.

Rate	Energy gap	Medium frequencies	Medium reorganization	Intramolecular mode	Electronic coupling
k_1	ΔG_1	ω_m=95cm^{-1}	λ_1=800	ω_c=1500 S_c=0.5	V_{PB}=20cm^{-1}
k_2	$\Delta G_2=\Delta G-\Delta G_1$	ω_m	λ_2=800	$\omega_c S_c$	V_{BH}=40cm^{-1}
k_{-1}	$-\Delta G_1$	ω_m	λ_2	ω_c, S_c	V_{BH}
k	ΔG	ω_m	λ=1600cm^{-1}	ω_c, S_c	$V_{PH}=\frac{V_{PB}V_{BH}}{\lvert\Delta G_1+\lambda_1\rvert}$
k_-	$-\Delta G$	ω_m	λ	ω_c, S_c	V_{PH}
k_Q	(200ps)$^{-1}$				
k_d	(300ps)$^{-1}$				
k_R	(1ns)$^{-1}$				
k_s	(20ns)$^{-1}$				
k_T	(2ns)$^{-1}$				

The energetic, electronic and nuclear parameters (Tables 1 and 2), which determine the primary rates (8)-(10), are taken from our recent work [45]. The (free) energy gaps for the chemically engineered and mutant RCs studied herein are summarized in Table 2. The rates for the surprisingly fast dimer internal conversion [49], the recombination of the ion pairs [50] and the quinone reduction rate [1-3] are taken from the experimental data and are summarized in Table 1. The solution of the kinetic equations (1)-(7) resulted in three lifetimes τ_j(j=1-3) and an amplitudes matrix $A_j^{(k)}$ (j,k = 1-3), with the temporal populations

$$[P^*](t) = \sum_{j=1}^{3} A_j^{(1)} \exp(-t/\tau_j) \quad , \tag{15a}$$

$$[P^+B^-H](t) = \sum_{j=1}^{3} A_j^{(2)} \exp(-t/\tau_j) \quad , \tag{15b}$$

$$[P^+BH^-](t) = \sum_{j=1}^{3} A_j^{(3)} \exp(-t/\tau_j) \quad . \qquad (15c)$$

Table 2. Energetic data for chemically engineered RC and for some of its mutants.

RC	References	$\Delta G_1(cm^{-1})$	$\Delta G_2(cm^{-1})$	$\Delta G(cm^{-1})$
NATIVE	42,45-47	- 500	-1500	-2000
NiB→B	14-16	-1500	- 500	-2000
H → B		(-2000)	(0)	(-2000)
Pheo→H	42	- 450	- 180	- 630
B → H		(- 500)	(0)	(- 500)
NiB→B Pheo→H		(-1500)	(1000)	(- 500)
'good' single site mutants	10,11, 17,18	-900 to 300	-1500	-2400 to -1200
triple H bonded mutant	19	(+1000) model	(-1500)	(- 500)

Calculations were performed for room temperature T = 300 K, using the electronic and energetic parameters previously advanced (Tables 1 and 2). In addition, model calculations were performed for a low temperature system at T = 20 K using the same parameters. The low temperature approximation does not account for the anisotropic thermal contraction, which may modify electronic, energetic, nuclear and static heterogeneity parameters (see section 3). Nevertheless, such low temperature simulations will be of use for the elucidation of the gross features of the ET kinetics.

3. Kinetic heterogeneity in the parallel mechanism

The parallel-sequential-superexchange scheme is now extended by the incorporation of the energy distribution of the ion pair states P^+BH^-

and P^+B^-H. The energy distribution functions $p(\Delta G_j')$ for the energy gaps $\{\Delta G_j'\}$ around a mean value ΔG_j, i.e., ΔG_1, ΔG_2 and $p(\Delta G')$ for $\{\Delta G\}$ around the mean value ΔG are taken to be Gaussian

$$p(\Delta G_j') = (2\pi\sigma^2)^{-1/2} \exp[-(\Delta G_j'-\Delta G_j)^2/2\sigma_j^2] \quad , \tag{16}$$

where σ_1 and σ_2 denote the distribution widths parameters around ΔG_1 and ΔG_2, respectively, while σ is the distribution width parameter around ΔG. Magnetic data for the recombination of the P^+BH^- have established that static heterogeneity of the energetics of the ion pair can be described in terms of Eq. (16) with $\sigma = 400\ cm^{-1}$. For the treatment of the N RC and of the mutants we have taken the energy levels of the ion pairs P^+B^-H and P^+BH^- to be correlated, i.e., $\Delta G_2' = -1500\ cm^{-1}$. The static heterogeneity parameters were taken to be temperature independent.

The kinetic analysis was conducted for the inhomogeneously broadened system. We calculated the lifetimes' vector $\tau(\Delta G_1') = \{\tau_j(\Delta G_1')\}$ and the amplitude matrix $\underset{\sim}{A}(\Delta G_1') = \{A_j^{(k)}(\Delta G_1')\}$ for each value of $\Delta G_1'$ within a discretized Gaussian distribution ($\sigma = 400\ cm^{-1}$) of 800 values.

The static heterogeneity results in a distribution of the lifetimes, which are characterized by the probability density of the distribution of the decay times of $^1P^*$

$$q(\tau) = \sum_j \int d(\Delta G_1')\delta(\tau-\tau_j(\Delta G_1'))\, A_j^{(1)}(\Delta G_1')p(\Delta G_1') \quad , \tag{17}$$

The time evolution of $^1P^*BH$ in the heterogeneous system is given by

$$P(t) = \int p(\Delta G_1')\, [P^*](\Delta G_1';t)d(\Delta G_1') \quad . \tag{18}$$

where $[P^*]\,(\Delta G_1';t)$ is calculated according to Eq. (15a) for the given values of $\Delta G_1'$. Making use of Eq. (17) the time evolution, Eq. (18), is given by

$$P(t) = \int d\tau\, q(\tau) \exp(-t/\tau) \quad . \tag{19}$$

To make contact with experimental reality we have calculated the quantum yield Y for charge separation

$$Y = \int k_Q[P^+BH^-](t)dt = k_Q \sum_{j=1}^{3} A_j^{(3)} \tau_j \ . \qquad (20)$$

To explore the central mechanistic issue of the interplay between the sequential and superexchange charge separation routes, we have calculated the branching ratio F_{sup} for superexchange, which is given by

$$F_{sup} = (1/Y) \sum_{j} (kA_j^{(1)} - k_- A_j^{(3)})\tau_j \ . \qquad (21)$$

where the rates k and k_- are defined by Eq. (2).

4. Kinetic modelling

4.1 The native RC

The static heterogeneity results, of course, in a distribution of lifetimes. Figure 2 portrays the probability density $q(\tau)$ vs τ, Eq. (17), for the native RC at T = 300 K and at T = 20 K. We note that $q(\tau)$ peaks at $\simeq \tau_1$, i.e., τ_1 = 3.5 ps at room temperature and τ_1 = 1.5 ps at T = 20 K, exhibiting the weak non-Arrhenius temperature dependence of the experimental nearly activationless ET. Longer time tails are exhibited with ~ 20% of the probability density for $\tau_1 \geq$ 6 ps at room temperature, while for T = 20 K about 40% of the probability density is manifested for $\tau_1 \geq$ 6 ps. Thus the effect of the distribution of lifetimes is considerably enhanced at low temperatures. This is apparent from the time dependence of the $^1P^*$ population P(t), which exhibits (Fig. 3) marked nonexponentiality, with dramatic long time tails being manifested at low temperatures. To explore the relative contributions of the sequential and the superexchange mechanisms, we calculated from Eq. (21) the branching ratios for superexchange. At room temperature (T = 300 K) F_{sup} = 0.02, with this minor contribution of superexchange originating from heterogeneity effects as for the homogeneous (σ = 0) model system F_{sup} = 0. We infer that for the native RC at room temperature the sequential mechanism dominates. At low temperatures, T = 20 K, we find F_{seq} = 0.1, whereupon the sequential mechanism still dominates but the superexchange makes a nonnegligible contribution. The 10% low-temperature contribution of

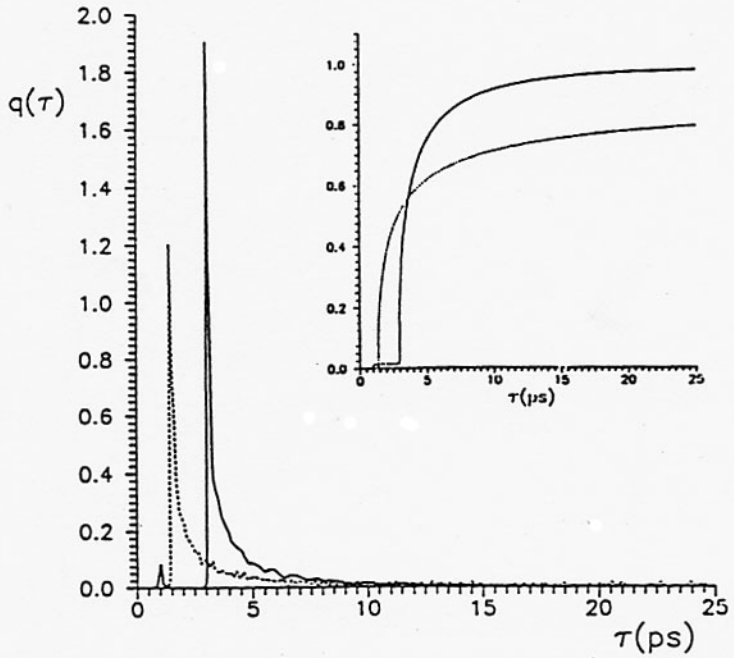

Fig. 2. The probability density $q(\tau)$, Eq. (17), of the $^1P^*$ relaxation time distribution for the native RC ($\Delta G = -2000\ cm^{-1}$, $\Delta G_1 = -500\ cm^{-1}$). The insert shows the accumulated value of $q(\tau)$. (1) Solid line T = 300 K. (2) Dashed line T = 20 K.

superexchange is intimately related to the appearance of the marked long-time tails in P(t) (Fig. 3), which originate from the superexchange channel. This conclusion is in accord with low temperature (T = 80 K) electric field effects on the polarization of the long time fluorescence (time scale 30-500 ps) from the native RC [54], which reveals the formation of the P^+BH^- ion pair via superexchange.

Of considerable interest is the long-time fluorescence (up to t ~ 1 ns) from native and from quinone depleted RCs [20,51-54]. Holzwarth et al [55] attempted to explain these phenomena in terms of a model based on the production of P^+BH^- via superexchange followed by its conformational relaxation. This model seems to be inconsistent with (i) the insensitivity of this "middle" fluorescence component to the quionone content [52] and (ii) the absence of nonphotochemical hole burning [56]. Therefore, this long-time direct fluorescence is attributed to static heterogeneity effects, which are limited by the internal conversion of $^1P^*$ ($k_d = (0.3\ ns)^{-1}$). Thus on the time scale up to ~ 1 ns direct dimer fluorescence competes with slow superexchange ET in the heterogeneous system. This physical picture implies that the long-

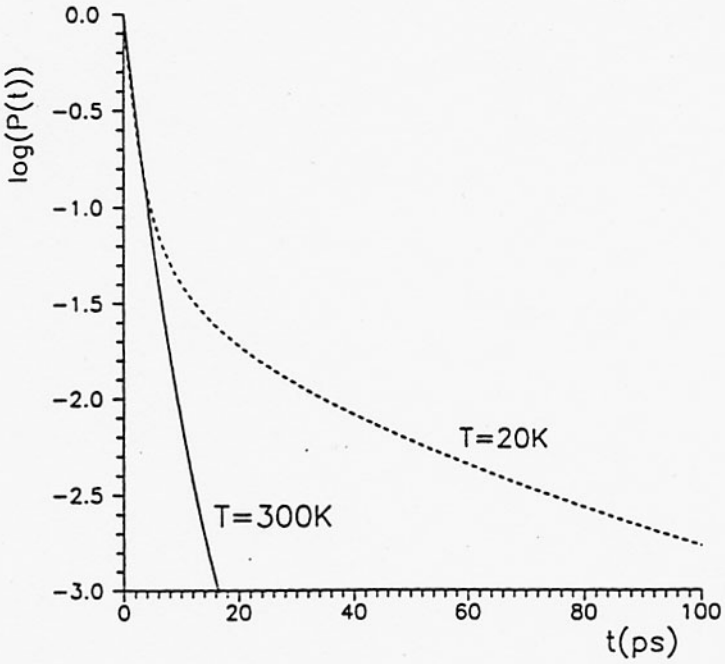

Fig. 3. Decay curves on a logarithmic scale (natural logarithm) of the $^1P^*$ population for the native RC (ΔG_1 = -500 cm^{-1}, ΔG = -2000 cm^{-1}) at T = 300 K, in the heterogeneous model: Solid line T = 300 K; dashed line T = 20 K.

time direct fluorescence (up to ~ 1 ns) should be similar for the native RC and in the Q depleted RC, as implied by our simulations (Fig. 4).

Another important experimental observable pertains to the quantum yield for primary charge separation, Eq. (20). Our kinetic modelling for the native RC at T = 300 K results in Y = 0.95, with the reduction of Y from unity being due to competition of ET with the internal conversion of the dimer (k_d) and the recombination of P^+BH^- (k_R). The pioneering work of Wraight and Clayton [57] gave Y = 1.02 ± 0.04, while recent experimental work [58,59] resulted in Y = 0.97 ± 0.02 at T = 300 K, in accord with our result. The quantum yield at low temperature (T = 20 K) is predicted to be reduced to Y = 0.90, manifesting more effective competition between internal conversion of $^1P^*$ and superexchange mediated long-time ET in the heterogeneous system.

We conclude that static heterogeneity effects at low temperature in the native RC are responsible for: (1) Superexchange (10%) contribution to the primary process. (2) Long-time (up to 1 ns) tails in the decay of $^1P^*$ manifesting superexchange ET. (3) Long-time direct

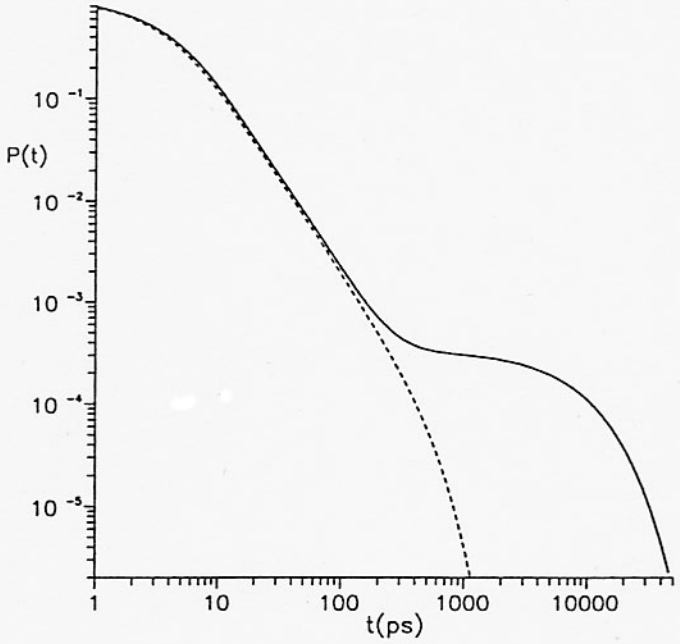

Fig. 4a. T = 300 K. Dashed line: native, and solid line: Q depleted.

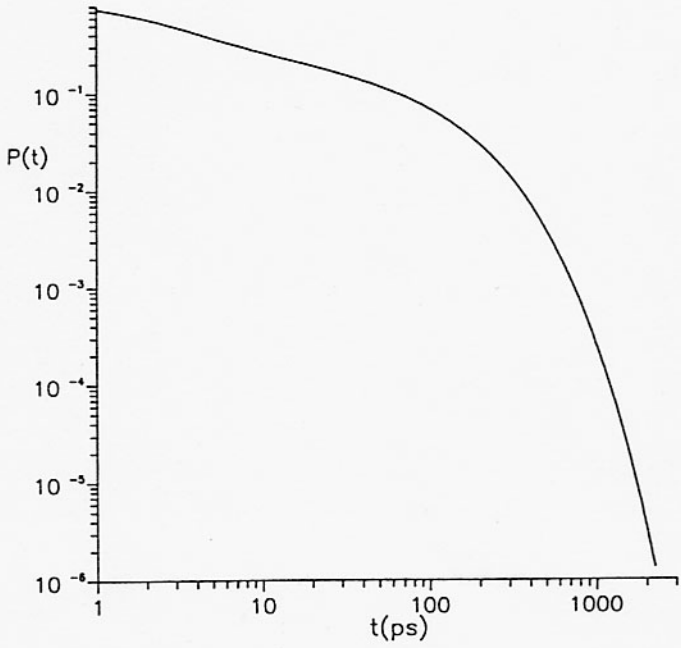

Fig. 4b. T = 20 K. The curves for native and for Q depleted RCs coincide.

Fig. 4. Kinetic modelling of long-time fluorescence decay in native and native-Q depleted RCs.

fluorescence due to competition between superexchange ET and internal conversion. (4) Reduction of the quantum yield for charge separation to $Y \simeq 0.90$.

4.2 The Ni-B RC

The replacement of the accessory bacteriochlorophylls B_A and B_B by the Ni-B in the photosynthetic RC of *R.sphaeroides R26* results in a drastic lowering of the energy of the $P^+(Ni\text{-}B)^-$ ion pair state (relative to P^+B^-) by about 1000 cm^{-1} [14]. This lowering is equivalent to $\Delta G_1 = -1500\ cm^{-1}$ for the Ni-B RC (Table 2). This chemically engineered RC provides the lowest value of ΔG_1. In this kinetic modelling we have accounted for quantum vibrational effects choosing a high frequency mode of $\omega_c = 1000\ cm^{-1}$ [47]. As before, we took $\sigma = 400\ cm^{-1}$. The recombination rates have been determined to be $k_T = 2\ (ns)^{-1}$ and $k_S = 20\ (ns)^{-1}$ [14]. The primary ET in this chemically engineered RC corresponds to the inverted region, where ET induced vibrational excitations of the quantum modes result in a very weak ΔG_1 dependence of the ET rate (Fig. 5). We predict that the primary ET rates of Ni-B ($\Delta G_1 = -1500\ cm^{-1}$) and of the native ($\Delta G_1 = -500\ cm^{-1}$) reaction centers (both with $\lambda_1 = 800\ cm^{-1}$) are close (Fig. 5). This prediction is borne out by the room temperature data for the Ni-B RC at T = 295 K which is characterized by a short decay component of $\tau_1 = 2.5$ ps (amplitude 69%) [15, 16], being very close to τ_1 for the native RC [39-42].

The effects of heterogeneity on the first step of ET are minor [14] as $|\Delta G_1| >> \sigma$. We expect that the heterogeneity effects are less marked for the Ni-B RC than for the native RC. This conclusion rests on the analysis of $q(\tau)$, Eq. (17) (Fig. 6) and P(t), Eq. (18) (Fig. 7), which reveal less pronounced long ($\tau \geq 6$ ps) temporal component than for the native RC (section (3.1)). In view of the minor heterogeneity effect ($|\Delta G_1| >> \sigma_1$) we expect that the low temperature long-time (t = 50-1000 ps) fluorescence is absent in the Ni-B RC (Fig. 7), in accord with experimental data. This result provides strong support for our physical picture for the long-time fluorescence tails in the native RC (section 3.1).

The new modified $H \rightarrow B$ RC, where the accessory bacteriochlorophyll(s) are substituted by bacteriopheophytin(s) (Table 2), is characterized by energetic parameters which are close to those of the Ni-B RC. Accordingly, the kinetics of ET in the $H \rightarrow B$ RC is expected to be similar to those predicted for the Ni-B RC.

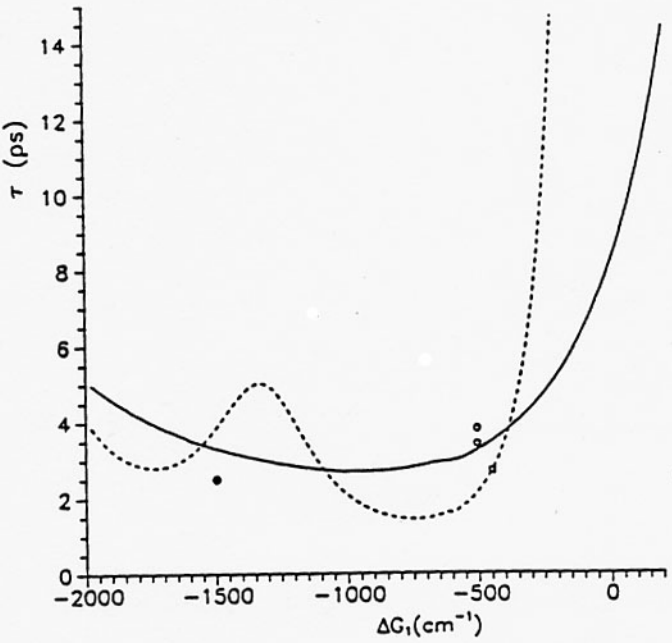

Fig. 5. The energy gap (ΔG_1) dependence of τ_1 in the absence of heterogeneity. Parameters from Tables 1 and 2 and ω_c = 1000 cm^{-1}. Solid line T = 300 K and dashed line T = 20 K. Experimental data for the short-time decay component of $^1P^*$ at T = 300 K are: Native RC (O - references 17,18 and [] - reference 11). Ni-B substituted RC (• - reference 15,16).

The marked lowering of ΔG_1 in the chemically engineered RC is of intrinsic interest in the context of the possibility of the induction of the primary charge separation across the B branch of the RC. The symmetry breaking, which induced ET across the A branch in the native RC, originates (at least) from the cumulative effects of reduced electronic coupling across the B branch and a high (unknown) value of the energy of the $P^+B_B^-$ ion pair state. Chemical substitution of B_B by Ni-B or by H will reduce the energy of the corresponding primary ion pair state, i.e., $P^+(Ni\text{-}B)_B^- H_B$ or $P^+H_B^- H_B$ across the B branch by ~ -1000 cm^{-1}. It remains to be seen whether this energy reduction is sufficient to break the symmetry breaking for the primary ET.

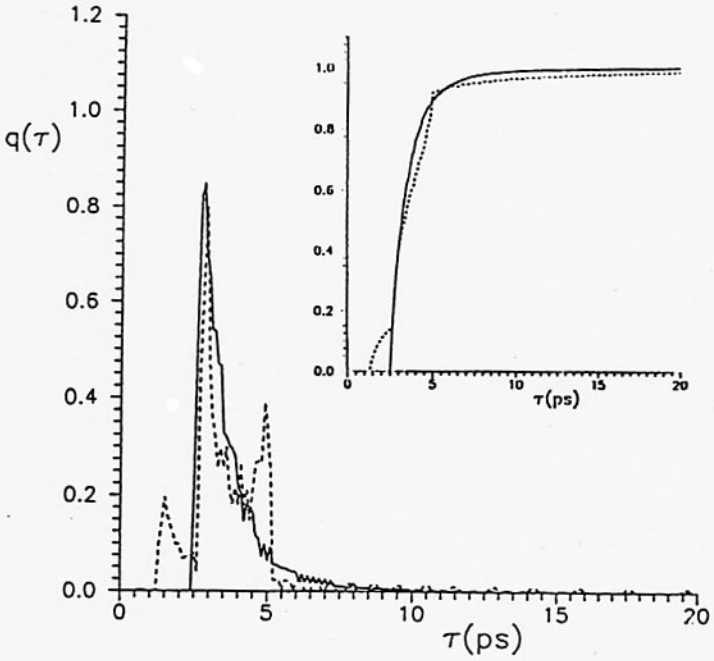

Fig. 6. The probability density $q(\tau)$ of the $^1P^*$ relaxation time distribution for the Ni-B substituted RC (ΔG_1=-1500 cm^{-1} and ΔG =-2000 cm^{-1}). The insert shows the accumulated value of $q(\tau)$. (1) Solid line T = 300 K. (2) Dashed line T = 20 K.

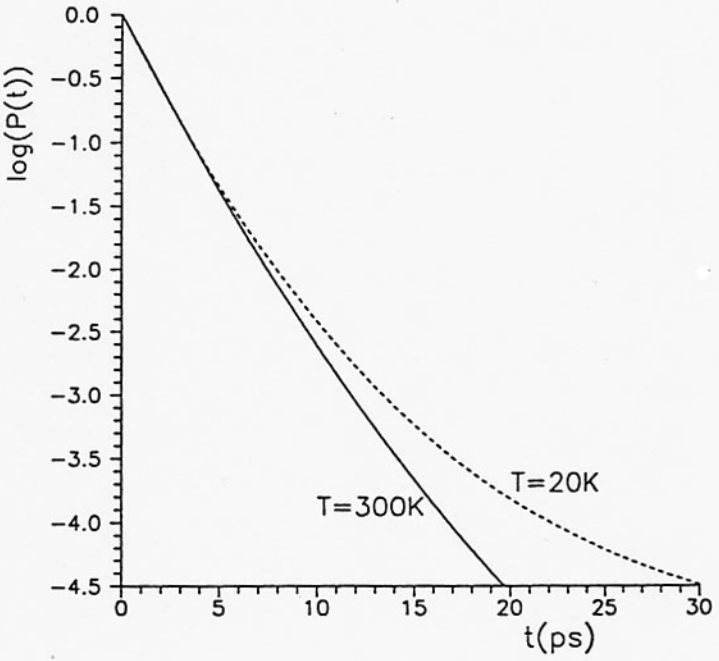

Fig. 7. Decay curve on a (natural) logarithmic scale of the $^1P^*$ population for the Ni-B substituted RC with heterogeneity.

4.3 Single-site and triple mutants

We shall consider now primary ET in 'good' [45,47] single-site mutants of *R.capsulatus* and *R.sphaeroides* [10,11,17,18] and the exploration of the primary ET in the triple hydrogen bond [LH(131) + LH)M160) + FH(197)] of *R.sphaeroides* [19]. The relevant energetics is presented in Table 2. Regarding heterogeneity effects, the energy levels of the P^+B^-H and P^+BH^- ion pair states were taken to be correlated with the same distribution (σ_1 = 400 cm^{-1}) and with the energy levels $\Delta G' = \Delta G_1' - 1500$ cm^{-1}.

The probability density q(τ), Eq. (17), for a series of model mutants with ΔG_1 = 0-1500 cm^{-1} (Fig. 8), reveals broad distributions. When the temporal decay of $^1P^*$ in the homogeneous system is dominated by a single exponential, q(τ) in the heterogeneous system peaks around $\sim \tau_1$. For ΔG_1 = -500 cm^{-1} (native RC) to 700 cm^{-1} the distribution q(τ) is skewed towards higher values of τ (Fig. 8). For ΔG_1 = 1000 cm^{-1}, when near degeneracy of the kinetic matrix prevails, a very broad distribution of q(τ) is exhibited, spanning the entire domain of τ. Finally, for the large ΔG_1 = 1500 cm^{-1} the distribution of the decay times peaks around the upper limit of k_D^{-1}, being skewed towards a low value of τ.

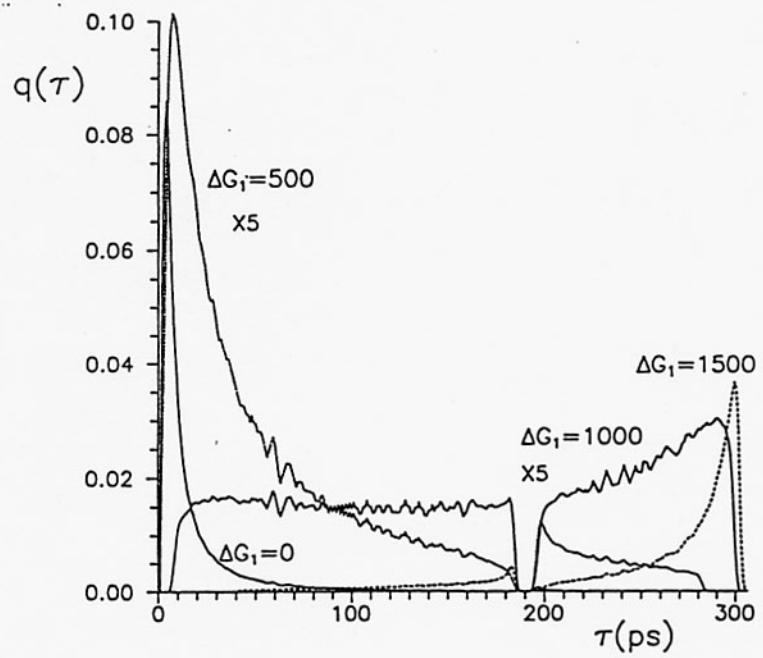

Fig. 8. The probability density q(τ) for the distribution of relaxation times of $^1P^*$ at T = 300 K for four values of ΔG_1 (ΔG_1 = 0 cm^{-1}, 500 cm^{-1}, 1000 cm^{-1}, 1500 cm^{-1}).

We have specified the (initial) dispersive decay of P(t), Eq. (19) (Fig. 9), in the heterogeneous system in terms of the lifetime $\tau(e^{-1})$ for which P(t) reaches the value of e^{-1}. In figures 10 and 11 we display the energy gap ΔG_1 dependence of the quantum yield for T = 300 K and for T = 20 K together with the characteristic lifetimes $\tau(e^{-1})$ for the decay of $^1P^*$ in the heterogeneous system. The values of $\tau(e^{-1})$ at T = 300 K span the range from 3.5 ps for $\Delta G_1 = -1000$ cm^{-1} (inverted region through $\tau(e^{-1}) = 4$ ps at $\Delta G_1 = -500$ cm^{-1} (native RC)) and then gradually increase towards $\tau(e^{-1}) = 200$ ps for $\Delta G_1 = 2000$ cm^{-1} (normal region). At low values of ΔG_1 the ET dynamics is dominated by the short sequential lifetimes k_1^{-1} and k_2^{-1}. On the other hand, for large values of ΔG_1 (> 1000 cm^{-1}) the ET dynamics is dominated by the $^1P^*$ internal conversion lifetime k_d^{-1} (Fig. 8).

We now turn to quantum yield data. The weak dependence of Y on ΔG_1 for $\Delta G_1 < 0$ indicates that for a large number of single-site mutants the primary charge separation is efficient at room temperature. Only for mutants with $\Delta G_1 \geq 0$ one expects a marked reduction of Y with increasing ΔG_1 in the range where the lifetime $\tau(e^{-1})$ exceeds 20 ps or so (Fig. 10), i.e., where internal conversion competes with charge separation. The effects of heterogeneity on Y at room temperature are small for $\Delta G_1 < 0$ becoming somewhat more marked (20%) at $\Delta G_1 = 0$-500 cm^{-1}, while in the extreme case of $\Delta G_1 = 1500$ cm^{-1} the heterogeneity enhances Y by a numerical factor of 2 (Fig. 10).

The energy gap dependence of the quantum yield at low temperatures T = 20 K (Fig. 11) is more pronounced, exhibiting a nearly linear decrease from Y = 0.90 for $\Delta G_1 = -500$ cm^{-1} (mimicking the native RC) to Y = 0.20 for $\Delta G_1 = 500$ cm^{-1}. At $\Delta G_1 = 1000$ cm^{-1} the yield further reduces to Y = 0.1, while photosynthetic charge separation at low temperatures is terminated for large $\Delta G_1 \geq 1500$ cm^{-1}. The heterogeneity effects on Y at T = 20 K are not pronounced for $\Delta G_1 < 500$ cm^{-1}, however, for large values of $\Delta G_1 > 500$ cm^{-1} the distribution of the energy gaps considerably enhances the quantum yield for charge separation, while the decay lifetimes (which are dominated by k_d^{-1}) are only weakly affected by heterogeneity. Finally, we turn to the mechanistic issues. The energy gap dependence of F_{sup} (Fig. 12) is classified according to the following ranges. (I) Dominance of the sequential mechanism, $F_{sup} \leq 0.1$. (II) Superposition of superexchange and sequential mechanisms, $0.1 < F_{sup} \leq 0.8$. (III) Dominance of the superexchange, $F_{sup} > 0.8$. At room temperature range (I) prevails for $\Delta G_1 < 500$ cm^{-1} and only at large $\Delta G_1 = 500$-1500 cm^{-1} range (II) is realized. At T = 300 K, heterogeneity effects are minor in range (I), while in range (II) heterogeneity effects enhance the contribution of the sequential channel (Fig. 12). At T = 20 K range (II) is realized in the

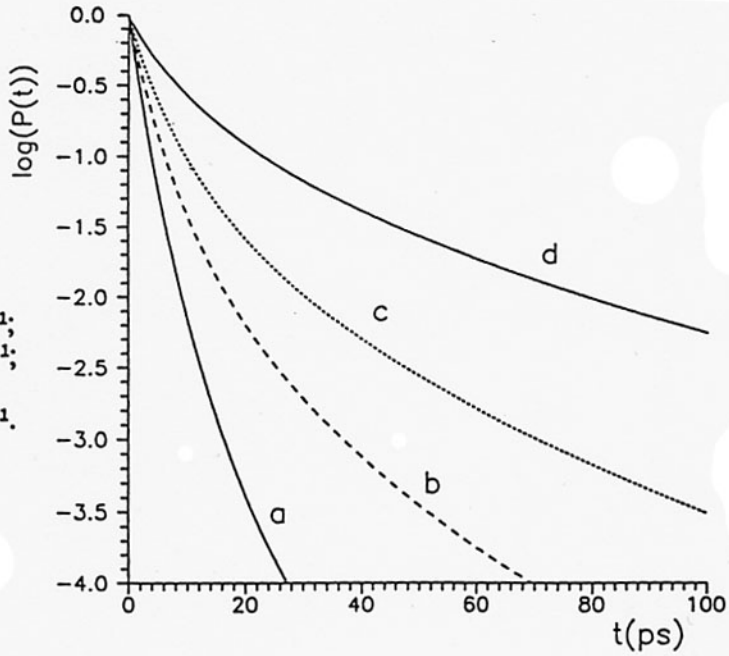

Fig. 9a.
a)ΔG_1=-500cm^{-1};
b)ΔG_1=-200cm^{-1};
c)ΔG_1= 0;
d)ΔG_1=+300cm^{-1}.

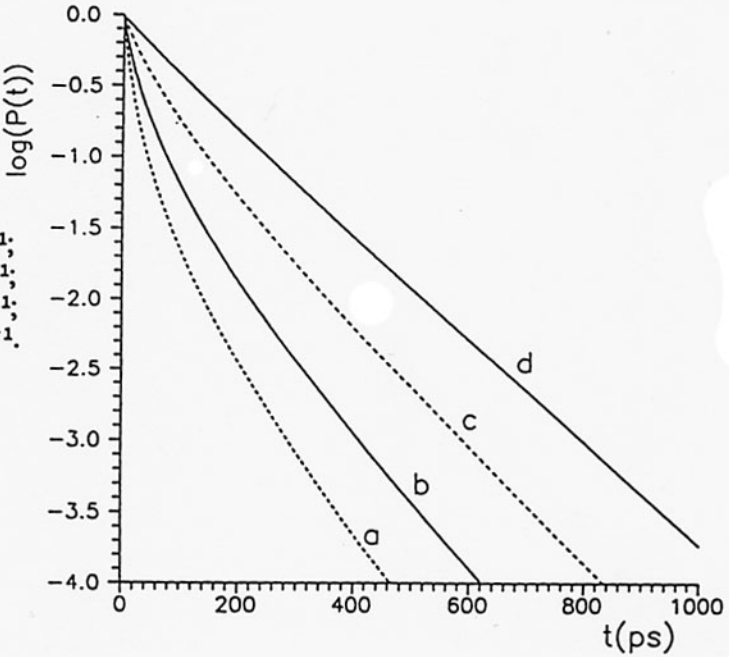

Fig. 9b.
a)ΔG_1=+ 500cm^{-1};
b)ΔG_1=+ 700cm^{-1};
c)ΔG_1=+1000cm^{-1};
d)ΔG_1=+1500cm^{-1}.

Fig. 9. Decay curves on a logarithmic scale (natural logarithm) of the $^1P^*$ population at T = 300 K, in the heterogeneous model.

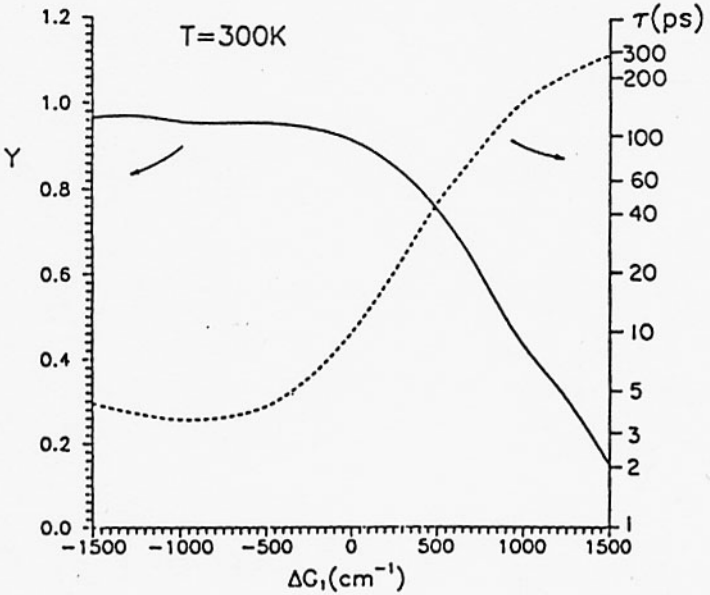

Fig. 10. The quantum yield (solid line) and the relaxation time ($\tau(e^{-1})$) of $^1P^*$ (dashed line) as function of the free energy gap ΔG_1 for the heterogeneous model at T = 300 K.

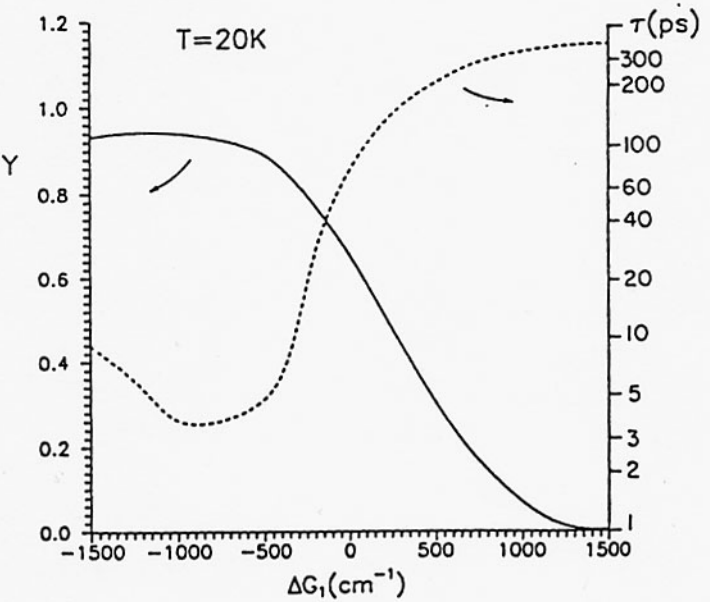

Fig. 11. The quantum yield (solid line) and the relaxation ($\tau(e^{-1})$) time of $^1P^*$ (dashed line) as function of the free energy gap ΔG_1 for the heterogeneous model at T = 20 K.

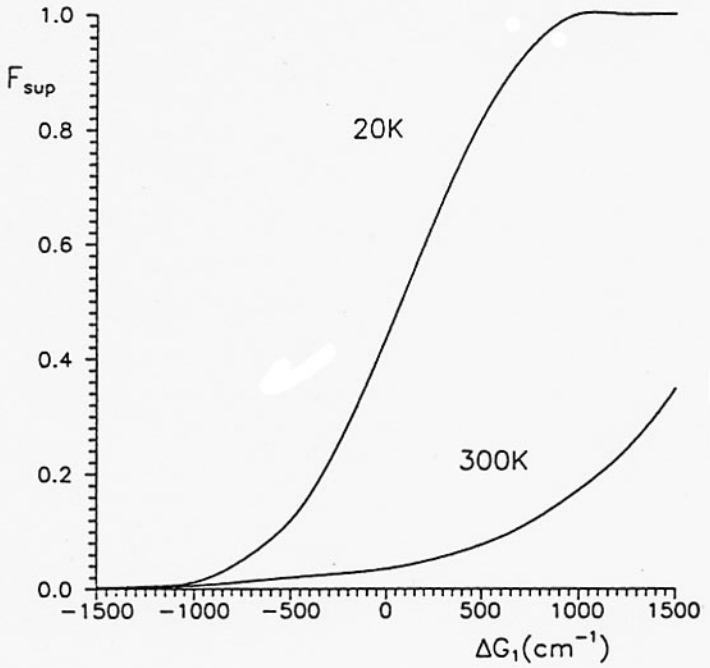

Fig. 12. The dependence of the branching ratio F_{sup} between the superexchange and the sequential rates on the (mean) energy gap ΔG_1 at T = 300 K (solid line) and T = 20 K (dashed line). F_{sup} is expressed as the fraction of the quantum yield that originates from the superexchange channel.

region $-500\ cm^{-1} < \Delta G_1 < 400\ cm^{-1}$. For $\Delta G_1 > 400\ cm^{-1}$ range (III) is exhibited at T = 20 K. Finally, at very large $\Delta G_1 \geq 1000\ cm^{-1}$ $F_{sup} \simeq 1.0$ and the superexchange channel exclusively dominates at T = 20 K, however, in this energy domain the quantum yield for charge separation is low.

What are the implications for mutagenesis? The most extensive information emerges from the kinetic modelling for the native RC and its single-site mutants at room temperature. The calculated ΔG_1 dependence of $\tau(e^{-1})$ exhibits a characteristic energy gap dependence (Fig. 10). The range $\Delta G_1 = -1000\ cm^{-1}$ to $-500\ cm^{-1}$ corresponds to the acitvationless region where $\tau(e^{-1})$ varies slowly, while a strong increase of $\tau(e^{-1})$ with increasing ΔG_1 is manifested for $\Delta G_1 = -500\ cm^{-1}$ to $300\ cm^{-1}$. Regarding the efficiency of the charge

separation, the quantum yield in the relevant range $\Delta G_1 = -900$ to 300 cm^{-1} is high, Y = 0.95-0.90, with Y only slightly decreasing with increasing ΔG_1. From the mechanistic point of view the charge separation for the native RC and its single site-mutants is dominated by the sequential route [range (I)].

Some heuristic information emerges on the charge separation in the native RC and its single-site mutants at low temperature (20 K). For mutants $\tau(e^{-1})$ increases with increasing ΔG_1 (Fig. 11) exhibiting a low-temperature energy gap dependence. In the range $\Delta G_1 = -300$ cm^{-1} to 300 cm^{-1}, $\tau(e^{-1})$ at 20 K is higher than the corresponding value at 300 K, so that these mutants exhibit an ordinary activated temperature dependence for the primary charge separation. The yield of the charge separation at 20 K reduces from Y = 0.9 for the native RC to Y = 0.4 for $\Delta G_1 = 300$ cm^{-1}. The role of superexchange is more pronounced at low temperatures, corresponding to the coexistence of the superexchange of sequential channels [range (II)]. For the single-site mutants, where $F_{sup} \simeq 0.1$-0.6 at T = 20 K, the effects of superexchange are marked.

The information which emerges from the kinetic modelling on the primary ET in the triple hydrogen bond mutant [19] is of considerable interest. The experimental values of the quantum yields for the charge separation in the triple mutant [19], i.e., Y = 0.4 at T = 300 K and Y = 0.10-0.15 at T = 20 K fitted well the kinetic modelling for $\Delta G_1 =$ 1000 cm^{-1}. For this large value of ΔG_1 the temporal decay of $^1P^*$ does not exhibit marked deviations from exponentiality (Fig. 9b) and the lifetimes $\tau(e^{-1})$ are long. The experimental lifetimes [19] are $\tau = 66$ ps at T = 300 K and $\tau = 290$ ps at 20 K. These results are in reasonable agreement with the lifetimes emerging from our kinetic simulations for $\Delta G_1 = 1000$ cm^{-1}, $\tau(e^{-1}) = 160$ ps for $\Delta G_1 = 1000$ cm^{-1} (while $\tau(e^{-1}) =$ 83 ps for $\Delta G_1 = 700$ cm^{-1}) at T = 300 K and $\tau(e^{-1}) = 270$ ps for $\Delta G_1 =$ 1000 cm^{-1} at 20K. In the triple mutant the effects of superexchange are marked ($F_{sup} \simeq 0.2$) at room temperature and dominant ($F_{seq} \simeq 1.0$) at low temperature.

References

1. The Photosynthetic Bacterial Reaction Center. Structure and dynamics, eds. J. Breton and A. Vermeglio (Plenum NATO ASI Series, New York, 1988).
2. Reaction Centers of Photosynthetic Bacteria, ed. M.E. Michel-Beyerle (Springer Verlag, Berlin, 1990).
3. The Photosynthetic Bacterial Reaction Center II, eds. J. Breton and A. Verméglio NATO-ASI series A (Life Sciences, Plenum Press, New York, 1992) vol. 237.

4. The Photosynthetic Reaction Center, eds. J. Deisenhofer and J.R. Norris (Academic Press, San Diego, 1993).
5. H. Frauenfelder, G.U. Nienhaus and J.B. Johnson, Ber. Bunsenges. Phys. Chem. 95 (1991) 272.
6. H. Frauenfelder and P.G. Wolynes, Phys. Roday 47 (1994) 58.
7. Spin Glasses and Biology (World Scientific Press, Singapore, 1992).
8. C. Kirmaier, D. Holten and W.W. Parson, Biochim. Biophys. Acta 810 (1985) 49.
9. C. Kirmaier and D. Holten, Proc. Natl. Acad. Sci. USA 87 (1990) 355, 2.
10. P. Hamm, K.A. Gray, D. Oesterhelt, R. Feick, H. Scheer and W. Zinth, Biochim. Biophys. Acta 1142 (1993) 99.
11. Y. Jia, T.J. DiMagno, C.-K. Chan, Z. Wang, M. Du. D.K. Hanson, M. Schiffer, J.R. Norris, G.R. Fleming and M.S. Popov, J. Phys. Chem. 97 (1993) 13180.
12. M. Du, S.J. Rosenthal, X. Xie, T.J. DiMagno, M. Schmidt, D.K. Hanson, M. Schiffer, J.R. Norris and G.R. Fleming, Proc. Natl. Acad. Sci. USA 89 (1992) 8517.
13. M.G. Müller, K. Griebenow and A.R. Holzwarth, Chem. Phys. Lett. 199 (1992) 465.
14. T. Häberle, H. Lossau, M. Friese, G. Hartwich, A. Ogrodnik, H. Scheer and M.E. Michel-Beyerle (this volume).
15. G. Hartwich, Ph.D. Thesis, TU München (1994).
16. G. Hartwich, M. Friese, H. Scheer, A. Ogrodnick and M.E. Michel-Beyerle, Chem. Phys. 197 (1995) 423.
17. J.C. Williams, R.G. Alden, H.A. Murchison, J.M. Peloquin, N.W. Woodbury and J.P. Allen, Biochemistry 31 (1992) 11029.
18. H.A. Murchison, R.G. Alden, J.P. Allen, J.M. Peloquin, A.K.W. Taguchi, N.W. Woodbury and J.C. Williams, Biochemistry 32 (1993) 3498.
19. N.W. Woodbury, S. Lin, X. Lin, J.M. Peloquin, A.K.W. Taguchi, J.C. Williams and J.P. Allen, Chem. Phys. 197 (1995) 506.
20. A. Ogrodnik, W. Keupp, M. Volk, G. Aumeier and M.E. Michel-Beyerle, J. Phys. Chem. 98 (1994) 3432.
21. G.J. Small, J.M. Hayes and R. Silbey, J. Phys. Chem. 96 (1992) 7499.
22. N.W. Woodbury, M. Becker, D. Middendorf and W.W. Parson, Biochemistry 24 (1985) 7516.
23. S.F. Fischer, I. Nussbaum and P.O.J. Scherer, in: Antennas and Reaction Centers of Photosynthetic Bacteria, ed. M.E. Michel-Beyerle (Springer, Berlin, 1985) p. 256.
24. A. Ogrodnik, N. Remy-Richter, M.E. Michel-Beyerle and R. Feick, Chem. Phys. Lett. 135 (1987) 576.
25. J.R. Norris, D.E. Budil, D.M. Tiede, J. Tang, S.V. Kolaczkowski, C.H. Chang and M. Schiffer, in: Progress in Photosynthetic

Research, ed. J. Biggins (Martinus Nijhoff, Dordrecht, 1987) vol. I, p. 1.4.363.
26. M.E. Michel-Beyerle, M. Plato, J. Deisenhofer, H. Michel, M. Bixon and J. Jortner, Biochim. Biophys. Acta 932 (1988) 52.
27. M. Bixon, J. Jortner, M. Plato and M.E. Michel-Beyerle, in: The Photosynthetic Bacterial Reaction Center. Structure and Dynamics, eds. J. Breton and A. Vermeglio (Plenum NATO ASI Series, New York, 1988) p. 399.
28. M. Plato, K. Möbius, M.E. Michel-Beyerle, M. Bixon and J. Jortner, J. Am. Chem. Soc. 110 (1988) 7279.
29. M. Bixon, M.E. Michel-Beyerle and J. Jortner, Isr. J. Chem. 28 (1988) 155.
30. M. Bixon, J. Jortner, M.E. Michel-Beyerle and A. Ogrodnik, Biochim. Biophys. Acta 977 (1989) 273.
31. R.A. Friesner and Y. Won, Biochim. Biophys. Acta 977 (1989) 99.
32. R.A. Marcus, Isr. J. Chem. 28 (1988) 205.
33. R. Haberkorn, M.E. Michel-Beyerle and R.A. Marcus, Proc. Natl. Acad. Sci. USA 70 (1979) 4185.
34. R.A. Marcus, Chem. Phys. Lett. 133 (1987) 471.
35. S.V. Chekalin, Ya.A. Matveetz, A.Ya. Shkuropatov, V.A. Shuvalov and A.P. Yartzev, FEBS Lett. 216 (1987) 245.
36. R.A. Marcus, Chem. Phys. Lett. 146 (1977) 13.
37. S. Creighton, J.-K. Hwang, A. Warshel, W.W. Parson and J. Norris, Biochem. 27 (1988) 774.
38. W. Holzapfel, U. Finkele, W. Kaiser, D. Oesterhelt, H. Scheer, H.U. Stilz and W. Zinth, Chem. Phys. Lett. 160 (1989) 1.
39. W. Holzapfel, U. Finkele, W. Kaiser, D. Oesterhelt, H. Scheer, H.U. Stilz and W. Zinth, Proc. Nat. Acad. Sci. USA 87 (1990) 5168.
40. C. Lauterwasser, U. Finkele, H. Scheer and W. Zinth, Chem. Phys. Lett. 183 (1991) 471.
41. T. Arlt, S. Schmidt, W. Kaiser, C. Lauterwasser, M. Meyer, H. Scheer and W. Zinth, Proc. Natl. Acad. Sci. USA 90 (1993) 11757.
42. P.M. Schmidt, T. Arlt, P. Hamm, H. Huber, T. Nägele, J. Wachtveitel, M. Meyer, H. Scheer and W. Zinth, Chem. Phys. Lett. 223 (1994) 116
43. M. Bixon, J. Jortner and M.E. Michel-Beyerle, Biochim. Biophys. Acta 1056 (1991) 301.
44. M. Bixon, J. Jortner and M.E. Michel-Beyerle, reference 3 (1992) 291.
45. M. Bixon, J. Jortner and M.E. Michel Beyerle, Chem. Phys. 197 (1995) 389.
46. A. Ogrodnik, M. Friese, P. Gast, A.T. Hoff and M.E. Michel-Beyerle, Biophys. J. (1966) in press.
47. M. Bixon, J. Jortner and M.E. Michel-Beyerle (this volume).

48. M. Bixon and J. Jortner, Chem. Phys. 176 (1993) 467.
49. U. Eberl, M. Gilbert, W. Keupp, T. Langenbacher, J. Siege, I. Sinning, A. Ogrodnik, S.J. Robles, J. Breton, D.C. Youvan and M.E. Michel-Beyerle, reference 15, p. 253.
50. M. Bixon, J. Jortner and M.E. Michel-Beyerle, Z. Phys. Chem. 180 (1993) 193.
51. A. Ogrodnik, Mol. Cryst. Liq. Cryst. 230 (1993) 35.
52. G. Hartwich, H. Lossau, A. Ogrodnik and M.E. Michel-Beyerle (this volume).
53. J.M. Peloquin, Jo Ann C. Williams, X. Lin, R.G. Alden, A.K.W. Taguchi, J.P. Allen and N.W. Woodbury, Biochemistry 33 (1994) 8089.
54. U. Eberl, A. Ogrodnik and M.E. Michel-Beyerle, Z. Naturf. 45a (1995) 763.
55. M.G. Müller, K. Griebenow and A.R. Holzwarth, Chem. Phys. Lett. 199 (1992) 465.
56. N. Raja, S. Reddy, S.V. Kolaczkowski and G.J. Small, J. Phys. Chem. 97 (1993) 6934.
57. C.A. Wraight and R.K. Clayton, Biochim. Biophys. Acta 333 (1973) 246.
58. M. Volk, G. Scheidel, A. Ogrodnik, R. Feick and M.E. Michel-Beyerle, Biochem. Biophys. Acta 1058 (1991) 217.
59. P. Müller, A. Ogrodnik and M.E. Michel-Beyerle (to be published).